Available online at www.sciencedirect.com
ScienceDirect
Journal of the European Ceramic Society 26 (2006) 3415–3423
www.elsevier.com/locate/jeurceramsoc

Fabrication and residual stresses characterization of novel non-oxide multilayer ceramics

D. Sciti [a,c,*], M. Nagliati [a,c], S. Tochino [b,c], G. Pezzotti [b,c], S. Guicciardi [a,c]

[a] *CNR-ISTEC, Institute of Science and Technology for Ceramics, Via Granarolo 64, I-48018 Faenza, Italy*
[b] *Department of Materials, Kyoto Institute for Technology, Matsugasaki, Sakio-ku, Kyoto 606-8585, Japan*
[c] *Research Institute for Nanoscience, RIN, Kyoto Institute of Technology, Sakyo-ku, Matsugasaki, Kyoto 606-8585, Japan*

Received 7 May 2005; received in revised form 26 September 2005; accepted 30 September 2005
Available online 14 November 2005

Abstract

A multilayer composite was produced by the tape-casting technique in the AlN–SiC–$MoSi_2$ system, coupling insulating and electrically conductive layers. The composite was highly dense and delamination-free. The values of residual stresses due to the coupling of layers of different composition were assessed using the indentation technique and Raman piezo-spectroscopy. The experimental techniques agreed in respect to the sign and magnitude of the residual stresses, revealing compression in the insulating layers and tension in the conductive layers. The experimental results were lower than the expected values calculated by lamination theory. The choice of the parameter values needed for the theoretical calculations appears to be critical from this point of view.

Keywords: Composites; (Raman piezo-)spectroscopy; Mechanical properties; Tape casting; Laminates; AlN; SiC; $MoSi_2$

1. Introduction

Laminar ceramic composites have been widely studied since they offer the possibility of obtaining superior properties in term of strength, fracture toughness and wear resistance; thanks to the design of specific architectures in which different laminated materials are coupled and the layers' thickness is carefully controlled.[1–6] However, it must be considered that, when coupling two different materials in a multilayer configuration, residual stresses can arise mainly due to the different thermal expansion of the materials. The magnitude of these residual stresses depends on the elastic and thermal expansion coefficients (CTEs) mismatch of the layers, the layers' thickness and the stress-free temperature.[1–3] In order to avoid cracking and delamination, a precise control of both the magnitude and distribution of the residual stresses is mandatory. In particular, an experimental assessment of these residual stresses can help to design better multilayer composites.

A number of techniques can be used to measure residual stresses in ceramic materials, including X-ray diffraction,[7,8] neutron diffraction,[9,10] indentation technique[11,12] and piezo-spectroscopic analyses.[4,5,13,14] In particular, Raman piezo-spectroscopy, due to its very small spot size (~1 μm), has already been shown to be a reliable technique for characterizing residual stress maps in alumina/zirconia multilayers.[4,5,15]

In this work, a new kind of non-oxide multilayer ceramic composite in the AlN–SiC–$MoSi_2$ system is presented. As a bulk material, this system has already shown remarkable room-temperature and high-temperature properties along with a high oxidation resistance up to 1500–1600 °C.[16–18] The main characteristic of this system is the ability to tailor electrical conductivity by varying the $MoSi_2$ content. Electro-conductivity measurements have shown that for $MoSi_2$ content higher than 25–30 vol.% the composite is electro-conductive with resistivity of the order of 10^{-3} Ω cm, whilst for lower $MoSi_2$ content (10–15 vol.%) the composite resistivity is over 10^2–10^3 Ω cm. Furthermore, these types of composites have been successfully produced by tape-casting technique[19] which should allow multilayer composites to be easily produced. One interesting application of these materials is in fact as heaters and igniters where, in most of these devices, thin layers

* Corresponding author. Tel.: +39 0546699748; fax: +39 054646381.
E-mail address: dile@istec.cnr.it (D. Sciti).

0955-2219/$ – see front matter © 2005 Elsevier Ltd. All rights reserved.
doi:10.1016/j.jeurceramsoc.2005.09.106

Table 1
Slurry composition (vol.%) at different X, Y and plasticizers ratio volume X: organic to inorganic ratio, Y: binder to plasticizer ratio

Formulation	Ceramic (vol.%)	Deflocculant (vol.%)	PVB (vol.%)	BBP + PEG (vol.%)	Solvent (vol.%)	X	Y	Plasticizers ratio
I	28.42	0.91	5.63	5.63	59.41	0.7	1.0	0.7:0.3
C	26.84	1.00	5.25	5.25	61.66	0.7	1.0	0.5:0.5

(∼100–200 μm) having different electrical resistivities are coupled.

In this contribution, homogenous and heterogeneous laminates in the AlN–SiC–$MoSi_2$ system are produced. In heterogeneous structures, electrically insulating layers are coupled to conductive layers and the resulting microstructure is studied. Macroscopic residual stresses developed in the heterogeneous composite are measured by an indentation technique and by Raman piezo-spectroscopy. Experimental results are then discussed and compared to theoretical models.

2. Experimental

2.1. Material preparation

The characteristics of the starting powders are the following: Hexagonal AlN, grade C (H.C. Starck, Germany), mean particle size 0.85 μm, oxygen content 0.25 wt.%; β-SiC (BF-12, H.C. Starck), mean particle size 0.15 μm, oxygen content 0.88 wt.%; tetragonal $MoSi_2$ (Aldrich, USA), mean particle dimension 2.7 μm, oxygen content 1 wt.% Y_2O_3, grade C (H.C. Starck, Germany). The as-received $MoSi_2$ powder was ball-milled for 120 h in ethanol and dried to reduce the mean particle diameter from 2.7 to 1.8 μm. The compositions in vol.% of the ceramic layers are the following:

$55AlN + 15SiC + 30MoSi_2$, labelled as C.
$80AlN + 10SiC + 10MoSi_2$, labelled as I.

Each composition was treated with 2 wt.% of Y_2O_3 as sintering aid. The powders were dispersed in an azeotropic mixture of methyl-ethyl-ketone and ethanol (MEK–EtOH, 66–34 vol.%) with 1 wt.% of deflocculant (Ep, Emphos PS 610, Crompton, France) and ball-milled with Si_3N_4 milling media. The binder (poly-vinyl-butyral PVB, B98, Monsanto, USA) and the plasticizers (polyethylene glycol PEG-400, Merck, Germany and benzyl-butyl-phtalate BBP, S160, Monsanto, USA) were subsequently added, according to the procedure described in ref. [19]. The formulations of the slurries are reported in Table 1. The formulation of composition C was set on the basis of the work reported in ref. [19]. The formulation of composition I adopted the same conditions, except for the plasticizers ratio, which was modified to favour the peeling away of the tape and to avoid adhesion phenomena on the support.

Circular samples with a thickness of 250 μm and a diameter of 40 mm were punched out from the as-cast green tape. Homogeneous laminates were obtained by stacking insulating or conductive monolayers, i.e. I/I . . . I/I and C/C . . . C/C, hereafter indicated as BI and BC. A heterogeneous laminated composite was produced alternating C and I layers with sequence I/I/C/I/C/I/C/I/C/I/I, hereafter indicated as ICI. A schematic diagram of the specimen's preparation is shown in Fig. 1. All the laminates were warm-pressed at 75 °C for 15 min with an applied pressure of 17 MPa and then heated at 80 °C for 15 min without pressure. The burnout stage (150 °C/h from 25 to 600 °C, 30 min of holding time) was chosen on the basis of previous thermogravimetric analysis.[19] Sintering was carried out in a graphite furnace, at 1850 °C for 30 min (heating up: 600 °C/h), under flowing nitrogen. In order to prevent dissociation of AlN, the green samples were placed in a powder bed with composition 80 wt.% AlN + 20 wt.% BN. The relative densities of the sintered samples were measured using Archimedes method. On polished surfaces, the microstructure was analysed by scanning electron microscopy (SEM, Cambridge S360, Cambridge, UK) and energy dispersive microanalysis (EDS, INCA Energy 300, Oxford Instruments, UK).

On the homogeneous laminates, BI and BC, the linear thermal-expansion coefficient (CTE) was measured with dilatometric tests (Netzsch Geraetebau Dil E 402, Germany) up to 1400 °C in air, with a heating rate of 5 °C/min. On the same samples, the electrical conductivity measurements were carried out by a four-probe DC method at room temperature, inducing a current in 2 mm × 2.5 mm × 25 mm bar specimens. The current and the voltage reading were detected at the same time with two different digital high-resolution multimeters. The conductivity values were determined from the electrical resistance measurement, taking into account the test leads distance and cross-sectional area of the samples.

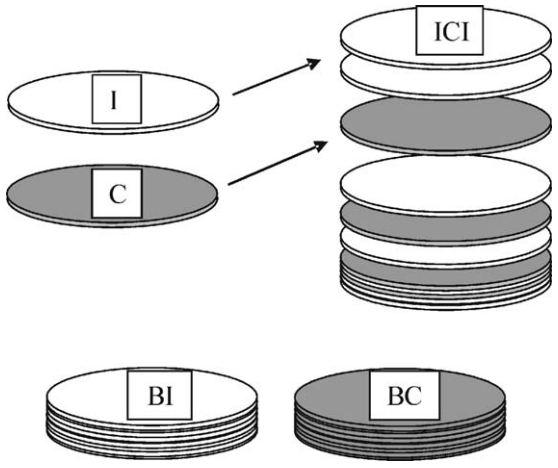

Fig. 1. Schematic of the laminates production. Legend: I: insulating layers; C: conductive layers; ICI: heterogeneous laminate; BI: homogeneous laminate containing I layers; BC: homogeneous laminate containing C layers.

2.2. Measurement of residual stress by indentation technique

The presence of a residual stress field in a material modifies the indentation crack length with respect to the length observed in the same stress-free material. The influence of residual stresses on the length of the indentation cracks is such that the true fracture toughness, K_{Ic}, of the material can be calculated by considering the contributions due to the indentation stress and the residual stresses field. For an indentation crack length c in a residual stress field σ_{res}, this implies[11]:

$$K_{Ic} = 0.016\left(\frac{E}{H}\right)^{1/2}\frac{p}{c^{3/2}} + y\sigma_{res}\sqrt{c} \quad (1)$$

where p is the applied indentation load, E and H the Young's modulus and the hardness of the material, respectively, and y is a constant related to the aspect ratio of the crack and can be taken as 1.29 for surface half-penny crack in a uniform stress field.[21] Vice versa, knowing the true fracture toughness of a material, for example, by measuring it in the stress-free state, and measuring the indentation crack length when the material contains a residual stresses field, the value of the residual stresses can be obtained by a non-linear regression of c over p according to Eq. (1).

For this purpose, the true fracture toughness of the layer I, which is also the external layer in the ICI laminate, was measured by Vicker's indentation technique on the polished top surface of the stress-free material BI with applied loads of 49.05, 68.67, 98.10 and 147.15 N using a Zwick hardness tester mod. 3212. Different values of applied load were used to assess the constancy of the K_{Ic} values, which should ensure that the crack system developed does not change by increasing the applied load. The formula of Anstis et al. was used for the calculation of K_{Ic}.[22] The Young's modulus of the layer I was calculated using the generalization of the Hashin and Strikman bounds for three-phase composites set up by Walpole,[23] taking literature values for the Young's modulus of the three constituent phases (AlN = 316 GPa,[24] SiC = 440 GPa,[25] $MoSi_2$ = 440 GPa[26]) and neglecting the contribution of any additional grain boundary phases (see Section 3.1). The value obtained for the I composition is 339 GPa. Then, indentation cracks were generated with the same loads on the outer layer of the ICI composite (plane YZ in Fig. 2). The indentation marks were introduced on the top surface of the ICI composite, which is under a biaxial stress state, and not in its cross-section (plane XY, Fig. 2), where the non-biaxial stress state would have generated an asymmetric cracks system. For the calculation of the residual stress, the non-linear regression of c over p was performed with commercial mathematical software (MATHEMATICA 5.0, Wolfram Research Inc., USA).

2.3. Measurement of residual stress by Raman piezo-spectroscopy

According to the studies carried out by Grabner,[20] when a material is under stress a shift of its characteristic Raman fluorescence peaks occurs. The relationship is given by the following tensorial expression:

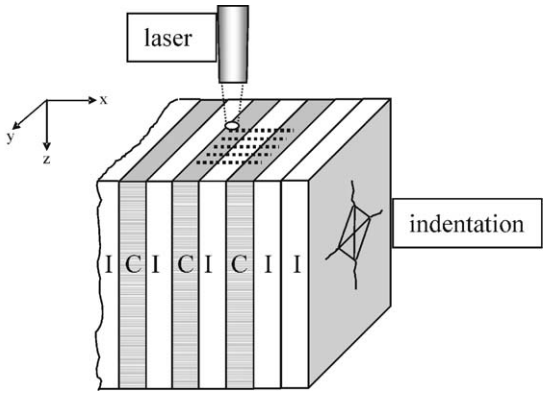

Fig. 2. Schematic of the Raman and indentation experiments carried out on the ICI material.

$$\Delta\nu = \Pi_{ij}\sigma_{ij} \quad (2)$$

where $\Delta\nu$ is the stress-induced peak shift, Π_{ij} is the piezo-spectroscopic tensor and σ_{ij} is the stress tensor. When the applied stress is uniaxial, the above equation reduces to a proportionality relation between the applied uniaxial stress and the shift of a selected Raman peak. As a first approximation, we will assume that under a hydrostatic stress field σ_h the relation can be written as:

$$\Delta\nu = \Pi_{av}\sigma_h \quad (3)$$

where Π_{av} is the average piezo-spectroscopic coefficient, $\Pi_{av} = 3\Pi_u$. Π_u is the piezo-spectroscopic coefficient measured under uniaxial stress.

For the Raman investigation, an Ar-ion laser operating at a wavelength of 488 nm was used as the excitation source. Specimens were placed on a mapping device (lateral resolution 0.1 μm), which allows very precise displacements on the specimen surface. The region of interest was selected using an optical microscope. Scattered frequencies were analyzed with a triple monochrometer equipped with a charge-coupled device camera. Bands from an Hg/Ne lamp were used as internal reference for spectral calibrations. The recorded spectra were examined by fitting with a Gauss-Lorentz mixed function using commercially available software (LABSPEC 4.02, Horiba/Jobin-Ivon). On the polished cross-section of the ICI composite (plane XY in Fig. 2), linear profiles were collected in steps of 1 μm and a laser spot size of about 1 μm (objective lens ×100). Five linear profiles were recorded, starting from the conductive layer (C), as schematically indicated in Fig. 2. With the same conditions, 7 μm × 7 μm maps were recorded in the bulk composites (BI and BC), which will be considered as zero-stress reference materials.

In order to determine the piezo-spectroscopic coefficient, Π_u, calibrations of spectral shift versus externally applied stress were carried out using a miniature four-point bending jig connected with a load-cell in which 3 mm × 4 mm × 20 mm bars cut from BC and BI reference materials were stressed. The bending jig was fixed in turn to a mapping device (lateral

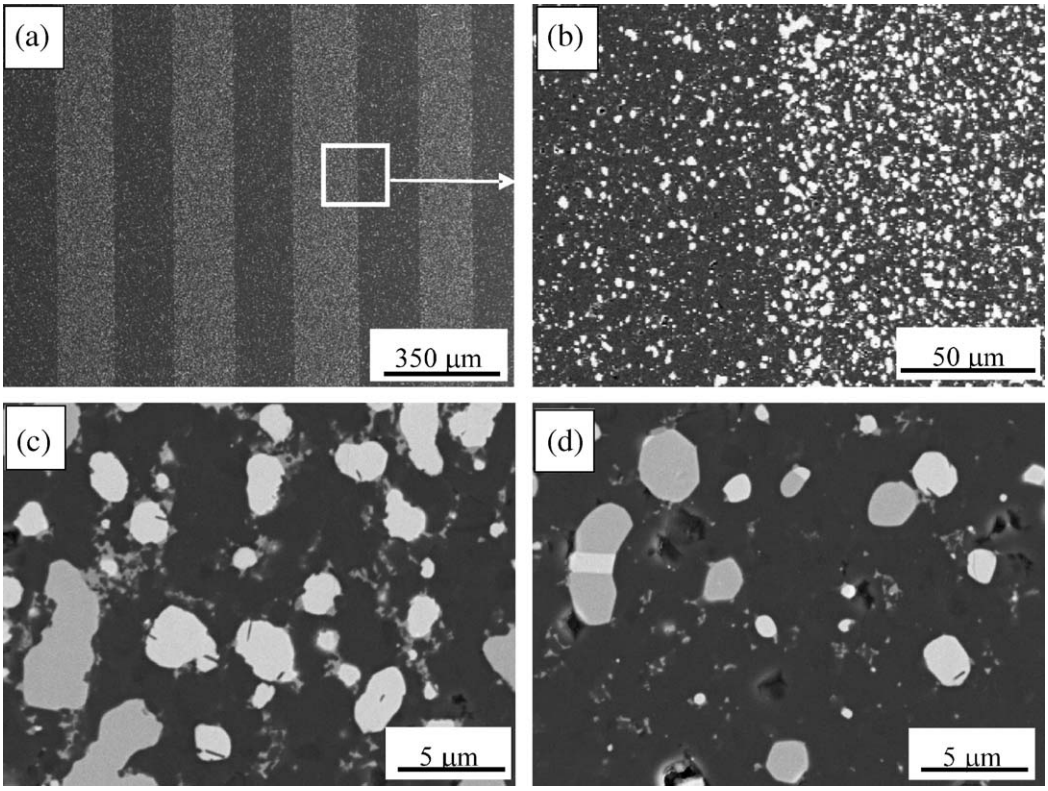

Fig. 3. Microstructure of the ICI laminate: (a) polished cross-section; (b) detail showing the interface between adjacent layers; (c) enlarged view of the conductive layers; and (d) enlarged view of the insulating layers. Bright contrast particles belong to the $MoSi_2$ phase.

resolution of 0.01 μm) connected to a personal computer to drive highly precise displacements in order to scan the bar lateral surface, i.e. from the bar edge under tension to the bar edge under compression.

3. Results

3.1. Microstructure and properties

Highly dense materials were obtained after sintering at 1850 °C, confirming the good sinterability of this non-oxide system. The relative densities of the BI and BC laminates were in the range 98–99%. The relative density of ICI laminate after sintering was >97%. All the theoretical densities were calculated with the rule of mixture, considering the starting nominal compositions. The presence of $MoSi_2$ particles is considered to be the key factor that improves the densification of this composite. $MoSi_2$ particles are in fact originally coated with an amorphous silica layer that enhances sintering kinetics acting as grain boundary lubricant and favouring the formation of liquid phase in the AlN–Y_2O_3–SiO_2 system.[16,17]

The main crystalline phases in the dense materials are the starting ones, as confirmed by previous studies.[16,17] Some microstructural features of the ICI composite are illustrated in Fig. 3a–d, showing a polished cross-section. Perfect adhesion was found between the layers and no delamination was observed through the composite (Fig. 3b), very likely due to the close similarity of composition of the layers containing the same starting phases. The final layers' thickness was around 170–180 μm for the inner layers and 370 μm for the outer layers (see Table 3).

In Fig. 3c and d, detailed views of the single layers are reported. The bright contrast particles are molybdenum disilicide and the grey regions consist of AlN and SiC phases, not distinguishable (even by backscattered imaging) due to the very close atomic number. The $MoSi_2$ particle distribution is homogeneous inside each layer. The mean $MoSi_2$ diameter evaluated by image analysis on polished surface is in the range 0.9–1 μm in both the I and C layers. Some aggregates of $MoSi_2$ particles are observed in the C layers due to the higher volumetric fraction. Intergranular phases consisting of crystalline YAG and/or amorphous silicate phases are present in all the systems. SEM observations evidence that the amount of secondary phases in I layers is considerably lower than in C layers. At the same time, I layers present a higher level of porosity. These two factors are again related to the $MoSi_2$ content and confirm that a higher content of this phase is beneficial for improving the densification. The microstructural features (not shown) of samples BI and BC are similar to those reported for I and C layers. Despite the lamination technique used, no traces of the junction between overlapping layers are observed, i.e. these layered composites resemble bulk materials. The mean $MoSi_2$ particle dimensions are in the range 0.9–1 μm, likewise for I and C layers.

As reported in Table 2, the BC laminate is a good conductor as a result of the interconnectivity of $MoSi_2$ particles, whilst in the BI sample, the amount of electro-conductive phase is too low to reach the percolation limit. As expected, the CTEs of the two materials are different as a result of the different starting

Table 2
Experimental values of CTE and electrical resistivity measured on the reference materials BI and BC.

Material	CTE 20–750 °C ($\times 10^{-6}$/°C)	CTE 20–1000 °C ($\times 10^{-6}$/°C)	CTE 20–1200 °C ($\times 10^{-6}$/°C)	Electrical resistivity (Ω cm)	Π_u (cm GPa^{-1})
BI	5.46	5.90	6.12	5×10^3	-1.80 ± 0.07
BC	6.14	6.54	6.77	3×10^{-3}	-0.90 ± 0.05

composition. The values are determined by the synergetic action of the three phases present. The mechanical properties of the heterogeneous laminated composite will be the subject of future work; however, just as an indication, the 4-pt bending strength of a pressureless sintered material (not cast) with the same composition as BC is about 380 MPa[18] and the fracture toughness, measured by indentation, is in the range 3–4 MPa m$^{1/2}$. These values can also be considered significant for the homogenous laminates, since their microstructure is not distinguishable from that of bulk materials. In contrast, the properties of the ICI composite are expected to change significantly due to the presence of the residual stress field.

3.2. Lamination theory

The values of residual stresses in a multilayer composite can be a priori calculated by considering the elastic constants, the thermal expansion coefficients and the thickness of the different layers along with the stress-free temperature by the equations of the lamination theory.[3] For a symmetrical composite with $2n + 1$ alternated layers, the equations which should be solved in order to obtain the values of the residual stresses are:

$$\varepsilon_i = \frac{1 - \nu_i}{E_i}\sigma_i + \alpha_i \Delta T = \text{constant} \quad (4)$$

$$\Sigma_i \sigma_i t_i = 0 \quad (5)$$

where σ_i is the stress developed in the layer of thickness t_i. Respectively, α_i, E_i and ν_i are the thermal expansion coefficients, the Young's modulus and the Poisson ratio of the ith layer. ΔT is the temperature range over which elastic stress develops due to thermal strain mismatch. The values of Young's modulus were calculated for I and C layers using the generalization of the Hashin and Strikman bounds for three phase composites set up by Walpole, as already mentioned. The Poisson's ratios were determined with the rule of mixture on the basis of starting compositions. The CTEs of the BI and BC materials are those reported in Table 2 for selected temperatures. A crucial parameter for the theoretical calculations is the stress-free temperature, i.e. the temperature below which stresses are accumulated elastically. This temperature is difficult to determine experimentally. Usually, it is taken somewhat lower than the sintering temperature, with 1200 °C being a quite common choice. However, in the present case, each individual layer contains $MoSi_2$ for which a brittle-to-ductile transition is known to occur at about 1000 °C.[26] Taking 1000 °C as the stress-free temperature, the calculated residual stresses in the ICI composite are −113 MPa in the I layers and +200 MPa in the C layers (Table 3).

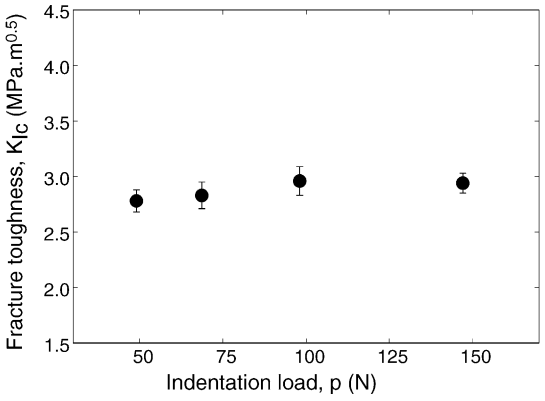

Fig. 4. Fracture toughness of the stress-free BI material as a function of the indentation load.

3.3. Indentation technique

The plot of true fracture toughness, K_{Ic}, of the stress-free BI material as a function of the indentation load is shown in Fig. 4. As can be seen, the value of fracture toughness is almost constant in the range of applied loads used, indicating that the crack system developed under the indentation marks does not significantly change by increasing the applied load. The crack lengths as a function of the indentation load in the stress-free BI material and in the stressed outer I layer of the ICI composite are shown in Fig. 5. The maximum crack length measured in the ICI composite was less than 220 μm, i.e. shallower than the external layer thickness. Applying Eq. (1), the regression of the indentation crack length on indentation load in the stressed layer gives −79 MPa as the value of residual stress in the outer I layer. As for the precision of this value, the standard error of ±4 MPa calculated by the regression can be assumed.

As shown in Section 3.2, the residual stress value in the conductive C layers, σ_{res}^{C}, can be calculated using the equilibrium

Table 3
Comparison of residual stress values with different techniques and according to theoretical models

Layer	Layer thickness (μm)	σ_{res} by Raman spectroscopy (MPa)	Indentation technique (MPa)	Theoretical (stress free $T = 1000$ °C) (MPa)	Theoretical (stress free $T = 750$ °C) (MPa)
I	Outer 370 ± 2, inner 175 ± 5	$-(62 \pm 3)$	$-(79 \pm 4)$	−113	−85
C	178 ± 10	$+(102 \pm 15)$	$+(140 \pm 4)$[a]	+200	+150

[a] By equilibrium criterion.

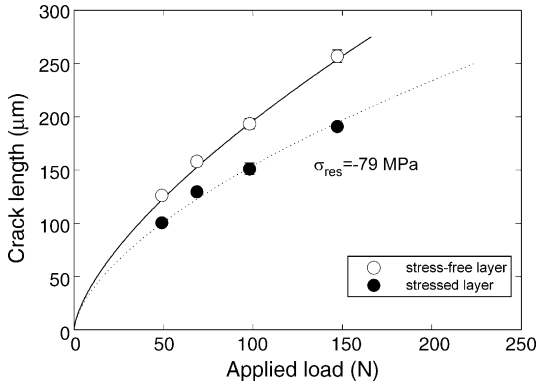

Fig. 5. Crack lengths as a function of the indentation load in the stress-free BI material and in the stressed outer I layer of the ICI composite.

criterion:

$$\sigma_{res}^{C} = -\frac{t_{tot}^{I}}{t_{tot}^{C}}\sigma_{res}^{I} \quad (6)$$

where σ_{res}^{I} is the residual stress in the I layer and t_{tot}^{I} and t_{tot}^{C} are the total thickness of I and C layers, respectively. With a σ_{res}^{I} of −79 MPa, the calculated value of σ_{res}^{C} is +140 MPa (Table 3).

3.4. Raman spectroscopy

The Raman spectra of these materials show the typical bands of hexagonal AlN at 656 cm^{-1},[27] β-SiC at 796 cm^{-1} [28] and tetragonal $MoSi_2$ at 430 cm^{-1} [29] (Fig. 6). Since the peaks of AlN and $MoSi_2$ had quite a low intensity, the β-SiC Raman band 796 cm^{-1} was chosen as stress sensor due to its sharpness. A representative Raman shift for the systems considered is illustrated in Fig. 7 a and b, where the SiC peak shifts of I and C layers of the ICI laminate are compared to the SiC peak positions in the reference BI and BC materials, respectively.

The calibration data for the SiC peak relative to the BI and BC samples are reported in Fig. 8a and b. The slopes of the regression lines, i.e. the piezo-spectroscopic coefficients, are −1.79 and −0.88 cm^{-1}/GPa for material BI and BC, respectively (Table 2). These values are significantly different from each other confirming that they are affected by the composition

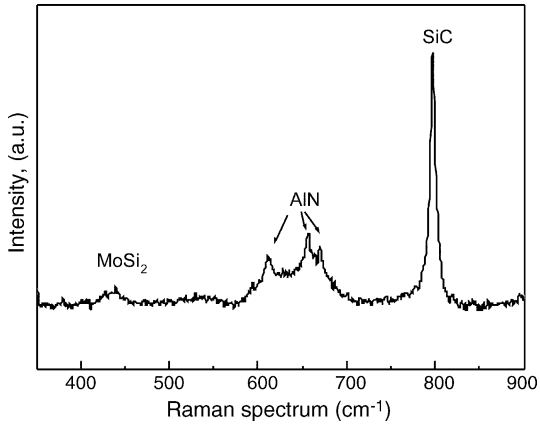

Fig. 6. Raman spectrum of the laminate.

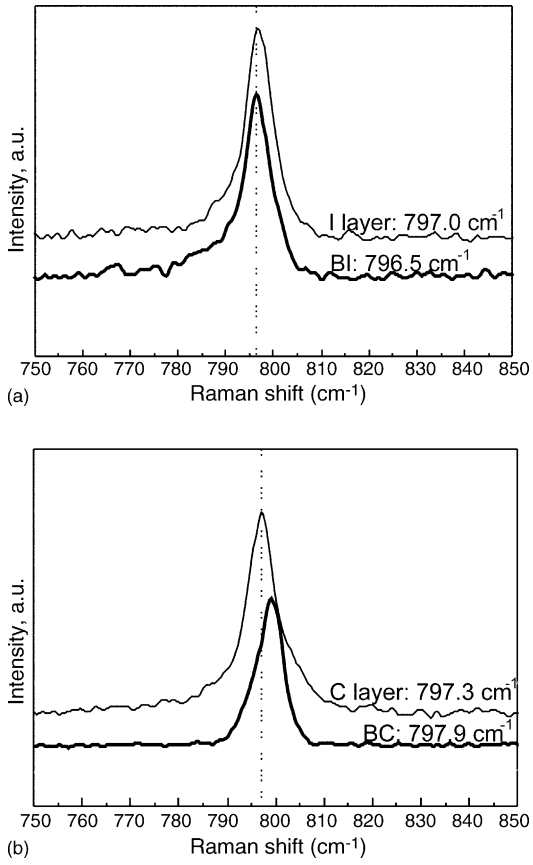

Fig. 7. Raman shift of the β-SiC Raman band (796 cm^{-1}) in (a) I layers of ICI in respect with BI reference material and (b) in C layers of ICI in respect with the reference BC material.

of their respective composite. These values are also different from the piezo-spectroscopic coefficient found for β-SiC single-crystal.[30] Using these values, the residual stresses profile of the multilayer composite was calculated according to Eq. (2). For the sake of clarity, in the materials of the present work the Raman laser has a very shallow penetration (see Section 3.5). Therefore, the line profiles in the ICI laminate were collected from a near-edge region where the stress state in non-biaxial due to the presence of a normal component.[5,31] This component, which has the opposite sign of the stress state inside the layer, vanishes going toward the core of the layer on a length comparable to the layer thickness,[5,31] namely 180 μm. Owing to this triaxial stress field, the constant Π_{av} in Eq. (2) was taken as three times Π_u and not two as in the case of a pure biaxial stress field.

The measured Raman shift in the I or C layers of the SiC phase is the result of both a lamination-induced macro-stress and a micro-stress due to the different CTEs of the constituent phases present in each individual layer (namely, AlN, SiC and $MoSi_2$).[32] However, having measured the piezo-coefficient of the SiC phase in bulk materials with composition C and I, i.e. the same composition of the layers forming the laminate composite, the SiC peak shift measured in the laminate composite is uniquely caused by the residual stresses induced by the lamination process. The resulting stress profile, averaged on the five scanning lines, is reported in Fig. 9. As expected, the insulating layers are under compressive stress while the conductive

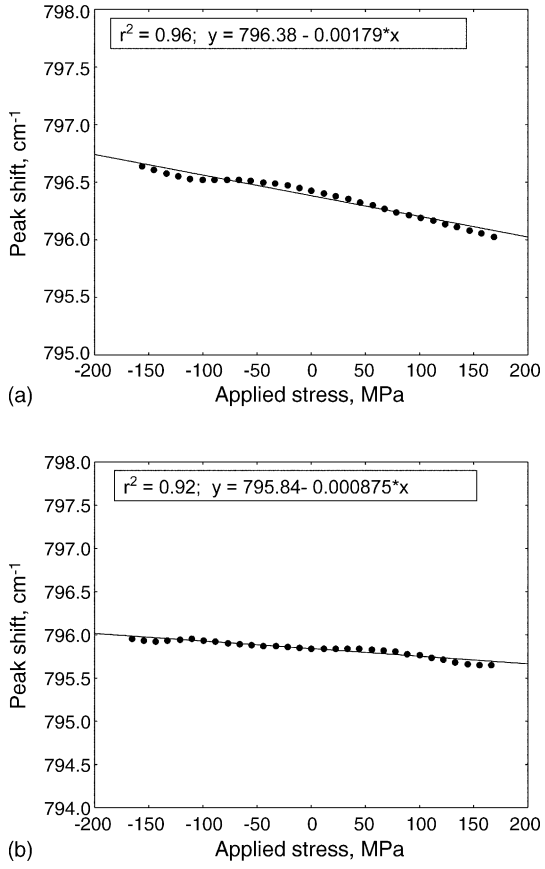

Fig. 8. Calibration data for the SiC peak in (a) BI and (b) BC reference material. The slopes of the regression lines represent the piezo-spectroscopic coefficients, Π_u.

layers are under tensile stress. The plot also clearly evidences that in the conductive C layers, the data are quite scattered with respect to the data in the I layers. This is very likely due to the higher volumetric fraction of the $MoSi_2$ phase which is a very strong absorbing phase as a previous study confirmed.[32] Further sources of experimental error can be, for example, microstructural inhomogeneities, such as the presence of silicate phases, particularly abundant in the conductive layers, and the presence of the microscopic stress field due to microstructural composition[32] that is superimposed to the lamination-induced macroscopic one. The average of the values reported in the plot of Fig. 9 are −62 MPa in the insulating layer and +102 MPa in the conductive one (Table 3). For the precision of these measurements, the standard error of the experimental values, either in I or in C layers, was considered (Table 3).

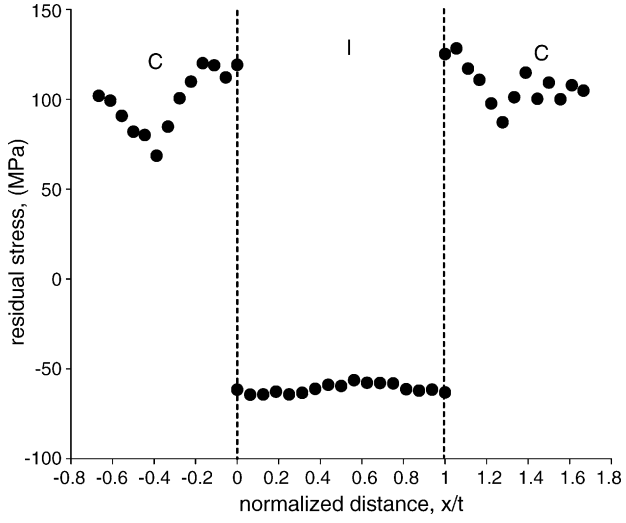

Fig. 9. Residual stress profile in the ICI laminate.

3.5. Comparison of the results

The experimental results and theoretical values are summarized in Table 3. Despite the different technique used, the experimental values obtained for the layers in compression agreed both in magnitude and sign of the residual stresses, with a difference between them of about 25%. For sake of precision, however, it must be clearly stated that results by the indentation technique are based on measurements carried out on the top surface of the multilayer composite where the stress field is purely biaxial, whilst Raman measurements were carried out on the cross-section where a normal component is present, as previously mentioned. In the materials of the present work the Raman laser has a very shallow penetration, therefore, the normal component, has a strong influence on the estimated values of residual stresses. This could be the justification for the slightly higher values measured by indentation with respect to those measured by Raman. The penetration depth of the laser in these materials can be evaluated to be less than a few micrometers, due to the strong absorption of the reinforcing $MoSi_2$ phase. This is based on the empirical observation that when the laser scans the $MoSi_2$ particles, the AlN and SiC Raman peaks are greatly reduced.[32] As a very rough approximation, one can estimate the mean penetration depth of the Raman laser in our composites as given by $1/(sn)$, where s is the cross-section between the laser and the particles and n is the number of particles per unit volume. Using the value of particles radius of 0.5 μm and the volumetric fraction of the reinforcing phase, the penetration depth is about 0.6 μm in the conductive layer and 1.3 μm in the insulating layers. Even if this were a very rough approximation, it would be difficult to think that the Raman laser could go deeper than the layer thickness, about 180 μm, where the normal component vanishes. Therefore, in these materials, Raman spectroscopy investigates the stress at the very surface of each layer.

The theoretical estimations were in any case higher than the experimental results (Table 3). For the Raman measurements, again the main reason could be the fact that the theoretical models consider the stress in the bulk of the laminate, where the stress field is purely biaxial, whilst Raman measurements are affected by the normal component.

Further sources of discrepancy between theoretical and experimental values could stem from the values used for the calculation themselves. In fact, the values of elastic constants were approximated without taking into account the presence of remnant phases in the microstructure of both C and I layers. In addition, the choice of the stress-free temperature is somehow ambiguous. The presence of amorphous silicate phases could

have contributed to lower the chosen stress-free temperature of 1000 °C, for example. Moreover, the brittle-to-ductile transition temperature of the $MoSi_2$, which was taken as 1000 °C, can be as low as 750 °C if the material has been previously prestrained.[33] This could be the case, since the $MoSi_2$ particles were ball milled for 120 h as indicated in the Experimental section. Inserting this latter value of stress-free temperature in Eq. (4), one obtains −85 MPa and +150 MPa as values of residual stresses in the I and C layer, respectively, which are closer to the experimental values, especially to the value obtained by indentation.

Lastly, it must be said that the difference between the theoretical estimations and the experimental values could have an explanation that is merely technological. In fact, in the calculation of the theoretical residual stresses it was not considered that the different layers could have different shrinkages during sintering. This shrinkage mismatch generates residual stresses in the multilayer composite that overlap the thermal residual stresses. It is likely that in our system the shrinkage mismatch was such as to reduce the residual thermal stresses calculated by the lamination theory.

4. Conclusions

Dense delamination-free multilayer composites were produced in the AlN–SiC–$MoSi_2$ system. Heterogeneous samples were produced, by alternating insulating and electrically conductive layers. Raman spectroscopy and an indentation technique were employed to evaluate the residual stresses among adjacent layers. Compressive residual stresses were found in the insulating layers whilst conductive layers were subjected to tensional stresses. The experimental techniques agreed in sign and magnitude of the residual stresses values. The comparison between experimental results and theoretical expectations provided evidence that the results of the theoretical model are greatly influenced by parameter values that are difficult to obtain experimentally, like the stress-free temperature. Moreover, the different shrinkages of the layers with different compositions could have superimposed sintering-derived residual stresses to lamination process-derived stresses. The presence of a compressive residual stress in the external layer of the heterogeneous material is expected to improve the mechanical properties of this system.

Acknowledgements

The two authors (D.S. and S.G.) gratefully acknowledge the financial support of the JSPS (Japan Society for the Promotion of Science) during their stay at RIN in Kyoto (J).

References

1. Rao, M. P. and Lange, F. F., Factors affecting threshold strength in laminar ceramic containing thin compressive layers. *J. Am. Ceram. Soc.*, 2002, **85**, 1222–1228.
2. Requena, J., Moreno, R. and Moya, J. S., Alumina and alumina/zirconia multilayer composites obtained by slip casting. *J. Am. Ceram. Soc.*, 1989, **72**, 1511–1513.
3. Chartier, T., Merle, D. and Besson, J. L., Laminar ceramic composites. *J. Eur. Ceram. Soc.*, 1995, **15**, 101–107.
4. Sergo, V., Room-temperature aging of laminate composites of alumina/3 mol%-yttria-stabilized tetragonal zirconia polycrystals. *J. Am. Ceram. Soc.*, 2004, **87**, 247–253.
5. Sergo, V., Lipkin, D. M., de Portu, G. and Clarke, D. R., Edge stresses in alumina/zirconia laminates. *J. Am. Ceram. Soc.*, 1997, **80**, 1633–1638.
6. Tarlazzi, A., Roncari, E., Pinasco, P., Guicciardi, S., Melandri, C. and de Portu, G., Tribological behaviour of Al_2O_3/ZrO_2–ZrO_2 laminated composites. *Wear*, 2000, **244**, 29–40.
7. Immelmann, S., Welle, E. and Reimers, W., X-ray residual stress analysis on machined and tempered HPSN-ceramics. *Mater. Sci. Eng.*, 1997, **A238**, 287–292.
8. Soares, M. R., Belmontea, M. and Silva, R. F., Low incident angle and classical X-ray diffraction analysis of residual stresses in diamond coated Si_3N_4. *J. Appl. Phys.*, 2003, **94**, 5633–5638.
[9]. Kupperman, D. S., Singh, J. P., Faber, J. and Hitterman, R. L., Application of neutron diffraction to the characterization of residual thermal strains in $YBa_2Cu_3O_{7-x}$/Ag. *J. Appl. Phys.*, 1989, **66**, 3396–3398.
10. Lukáš, P., Vrána, M., Mikula, P., Vleugels, J., Anné, G. and Van der Biest, O., Neutron diffraction study of the phase-specific stresses in graded alumina/zirconia ceramics. *Physica B*, 2004, **350**, e517–e520.
11. Widjaja, S., Jakus, K., Ritter, J. E., Atri, R. and Battacharaya, S., Residual surface stress by localized contact creep. *J. Mater. Res.*, 1997, **12**, 210–217.
12. Zhang, T.-Y., Chen, L.-Q. and Fu, R., Measurements of residual stresses in thin films deposited on silicon wafers by indentation fracture. *Acta Mater.*, 1999, **47**, 3869–3878.
13. De Wolf, I., Micro-Raman spectroscopy to study local mechanical stress in silicon integrated circuits. *Semicond. Sci. Technol.*, 1996, **11**, 139–154.
14. Dietrich, B. and Dombrowski, K. F., Experimental challenges of stress measurements with resonant micro-Raman spectroscopy. *J. Raman Spectrosc.*, 1999, **30**, 893–897.
15. Micele, L., Pezzotti, G., de Portu, G. and Sekiguchi, Y., Measurements of residual stress distributions in Al_2O_3/3Y-TZP multilayered composites by fluorescence and Raman microprobe piezo-spectroscopy. *Acta Mater.*, 2005, **53**, 1511–1520.
16. Sciti, D., Guicciardi, S., Melandri, C. and Bellosi, A., High-temperature resistant composites in the AlN–SiC–$MoSi_2$ system. *J. Am. Ceram. Soc.*, 2003, **86**, 1720.
17. Sciti, D. and Guicciardi, S., Microstructure and mechanical properties of novel ternary electroconductive ceramics. *J. Mater. Res.*, 2004, **19**, 3343–3352.
18. Krnel, K., Sciti, D. and Bellosi, A., *J. Eur. Ceram. Soc.*, 2003, **23**, 3135.
19. Roncari, E., Pinasco, P., Nagliati, M. and Sciti, D., Tape casting of AlN–SiC–$MoSi_2$ composites. *J. Eur. Ceram. Soc.*, 2004, **24**, 2303–2311.
20. Grabner, L., Spectroscopic technique for the measurement of residual stress in sintered Al_2O_3. *J. Appl. Phys.*, 1978, **49**, 580.
21. Murakami, Y. ed., *Stress Intensity Factors Handbook*, *Vol. 1*. Pergamon Press, Oxford, 1987, p. 42.
22. Anstis, G. R., Chantiful, P., Lawn, B. R. and Marshall, D. B., *J. Am. Ceram. Soc.*, 1981, **64**, 533.
23. Walpole, L. J., On bounds for the overall elastic moduli of inhomogeneous systems. *J. Mech. Phys. Solids*, 1966, **14**, 151.
24. Talwar, D. N., Sofranko, D., Mooney, C. and Tallo, S., Elastic, structural, bonding and defect properties of zinc-blende BN, AlN, GaN, InN and their alloys. *Mater. Sci. Eng.*, 2002, **B90**, 269–277.
25. Shackelford, J. F. and Alexander, W., ed., *CRC Materials Science and Engineering Handbook*. CRC Press, Boca Raton, 2001, p. Fl.
26. Jang, Y.-L. and Lavernia, E. J., Review, processing of molybdenum disilicide. *J. Mater. Sci.*, 1994, **29**, 2557–2571.
27. Ichimaru, H. and Pezzotti, G., Raman microprobe mapping of residual and bridging stress fields in AlN ceramics. *Mater. Sci. Eng.*, 2002, **A326**, 261–269.
28. Olego, D. and Cardona, M., Temperature dependance of the optical phonons and traverse effective charge in 3C–SiC. *Phys. Rev. B*, 1982, **25**, 3889–3896.

29. Srinivas, G. and Vankar, V. D., Raman spectroscopy of polycrystalline molybdenum silicide thin films. *Mater. Lett.*, 1997, **30**, 209–215.
30. Colombi, C. L., Gregori, G., Lughi, V., Rossi, A. and Sergo, V., Piezo-specroscopy: a materials science perspective. *Recent Res. Dev. Appl. Spectrosc.*, 1999, **2**, 243–272.
31. Kirchner, H., Conway, J. and Segall, A. E., Effect of joint thickness and residual stresses on the properties of ceramic adhesive joints: I, finite elements analysis of stresses in joints. *J. Am. Ceram. Soc.*, 1987, **70**, 104–109.
[32]. Sciti, D., Guicciardi, S., Celotti, G., Tochino, S. and Pezzotti, G., Analysis of residual stresses in novel electroconductive composites. *Appl. Phys. A*, 2006, **82**(2), 317–324.
33. Gibala, R., Chang, H. and Czamik, C. M., *Mater. Res. Soc. Symp. Proc.*, 1994, **322**, 175.